Experimental and numerical investigation of high-pressure jetting fluids impinging on submerged hard rock under deep geothermal downhole drilling conditions

John-Paul Latham[1], Jiansheng Xiang[1], Laurent Gerbaud[2], Hedi Sellami[2], Naveen Velmurugan[2], Alexandre Kane[3], Juan Yang[3], Terence Coudert[3], Hualin Liao[4], Haujian Wang[4]

[1] Imperial college London, Department of Earth Science and Engineering, SW7 2BP, London, UK

[2] ARMINES, 60 Bd Saint Michel 75272 Paris Cedex 6, France

[3] SINTEF, Richard Birkelands vei 2 B Trondheim, Norway

[4] China University of Petroleum, No. 66, West Changjiang Road, Huangdao District, Qingdao, China, 266580

j.p.latham@imperial.ac.uk

Keywords: High pressure water-jet drilling (HPWJ), impinging pressure, numerical model, simulation.

ABSTRACT

Hybrid drilling technology under development in the EU project 'ORCHYD' exploits peripheral groove cutting by high pressure water jet or drilling fluid jet to directly assist rate of penetration (ROP) of rotary percussive hammers. Numerical simulation with IC-FERST code applies non-Newtonian fluids solvers together with rotating boundary conditions applicable to the geometry of jetting experiments with realistic bottom-hole back pressures. In this work we focus on simulating jet configurations designed to deliver impinging pressures more than 100 MPa above back pressure, generated by drilling fluid circulation from the surface under deep (~5 km) in-situ conditions, with the aim of jetting hard rock such as granites. Impinging pressures are discussed in their role as a proxy for depth of groove cut and effectiveness in pre-conditioning rock for ease of hammer drilling. Hence, in future work, a more reliable and realistic pressure boundary condition will be used to model the solid destruction taking place for different rocks as the groove is cut.

This paper demonstrates the high levels of confidence that can be placed on the results of the HPWJ simulations of flow and distributions of jet pressure modelled with IC-FERST, based on similarities with theory and comparisons with alternative CFD methods. Furthermore, preliminary results from HPWJ experiments are reported for a novel design of a rugged high-pressure sensor for use in the high confining pressure rig modified for jetting tests and performed in the ARMINES laboratory. The destruction of two granite rock samples by such impinging pressures and the carving out of contrasting incipient grooves are illustrated.

1. INTRODUCTION

The idea that water jets might assist mechanical drilling has been around for half a century (Bobo 1963). Waterjet hybrid drilling research was reviewed by Stoxreiter et al., (2018) together with their early results on kerf cutting experiments as part of a project to develop an alternative drilling system within the H2020 EU research project "ThermoDrill". Recognizing a hybrid system would need to operate with a certain rate of rotation of the bit, a measure of success of the jet's power to assist ROP was given by the depth of a groove or mass of material removed per unit time by the traversing jet (Stoxreiter et al., 2018).

For deep hard rock drilling, the overwhelming evidence is that kerfing any groove to a depth, which assists drilling, is much more difficult because of the role of higher bottom hole back pressures (~50 MPa at 5 km depth). From simple theory, the increase in bottom hole drill fluid pressures generates increasing rock confinement and hence stress states are further removed from the rock's critical failure envelope criteria. Furthermore, experiments performing high pressure jetting into submerged rocks with a range of back pressures (Kolle, 1987; Poláček and Janurová, 2017; Stoxreiter et al., 2018) corroborate this theoretically predicted effect. However, the experiments suggest that it is possible to overcome 50 MPa of backpressure and the resistance to fracture of tough rocks like granites if: (i) a jet is from a nozzle chamber pressure with at least 220 MPa for the case of 50 MPa back pressure, (ii) there is enough power at the rock surface, and (iii) the jet does not transverse too fast.

The need for safe operational pressures delivered from any surface works and inevitable pressure losses from pipe friction over great drilling depths means that the development of down-hole pressure intensification systems that can put sufficient power into the jet at ~4-6 km depths, has become a hot topic worldwide.

ORCHYD partner China University of Petroleum (UPC) is one such group pioneering intensification systems (Liao et al., 2015) with expertise in modelling the pressures and velocities achievable by different downhole pressure intensifier designs harnessing the energy in the drill-string and fluids.

This paper deals with the fluids part and sets the scene for further use of a rotating localised pressure boundary condition method for the rock fracture and chip removal simulation in future solids modelling work.

2. BACKGROUND

To understand HPWJ in submerged impinging plate geometries, the conical jet theory momentum solution for turbulent jets of Schlichting and Gersten, (1979) are widely referenced together with the experiments of Hussein et al., (1994). The loss of jet velocity axially and radially in the air following a self-similar bell-like set of curves is generally considered applicable to submerged liquid flows for cases of similar Reynolds number (Re) and therefore flow regime, for turbulent jets. Re, which characterises the ratio between inertia and viscous forces can be estimated easily for a water jet at 20 ^{o}C, with the density of 1000 kg/m^3, a dynamic viscosity of 1 mPa.s and orifice diameter of 1 mm if we deduce the jet average velocities from nozzle chamber pressures. For average nozzle velocities of interest of 450 to 700 ms^{-1}, Re ranges from 450,000-700,000 (i.e., strongly turbulent).

To directly compare HPWJ simulated flows and pressures for submerged water jets with experimentally created flow fields for a validation study, Particle Image Velocimetry (PIV) could be used, but this is far from straight forward to set up for jetting scenarios of interest. Jasper et al., (2021) recently performed PIV to measure HPWJ velocity distributions using two different nozzles, one generating cavitation inside the nozzle. The scenarios tested looked at different back pressures but did not include cases relevant to where the jet orifice is at low stand-off distances from the domain wall. Another experimental approach is to mount pressures sensors directly in the path of the jet. Most success has been achieved with piezoelectric film (PVDF) sheets e.g., Jegaraj and Babu (2016); but these are prone to be damaged by the exceptional pressures of jets striking the sensor components, especially studies focussed on pulsed jets and the water hammer effect (see Dehkhoda and Hood, 2013). A more robust sensor system is therefore required to evaluate experimentally produced HPWJs to build confidence in results obtained by CFD especially in non-axisymmetric and complex geometries with very high Re and strongly turbulent models.

Industrial applications of HPWJ consider water jets exiting a specific chamber and nozzle geometry into air, usually focusing on thermal transfer. One recent study on the erosive scouring action on subaqueous sediments by Wang et al., (2020) stands out as relevant and reports Wray-Argawal turbulence capturing CFD results. Their study domain, while using a much larger diameter jet pipe of D = 20 mm and lower velocities of about 1 ms^{-1}, considered the Re range of flows of 11,700 ≤ Re ≤ 35,100 – somewhat below those expected to be delivered in the ORCHYD project (say, 450,000 to 700,000). The standoff distance effect on impinging pressure was studied by bringing the central pipe outlet further and further into a large rectangular computational domain of stagnant water with depth H = 8D, with distant outflow boundaries and the full water depth H_w = 12D. As stand-off distance divided by outlet width, H/D increases from 1, their results predict a steadily accelerating decline of the maximum impinging pressure by a factor of 2 when H/D = 8. The velocity profile for outflow at the exit of the pipe is assumed to be a fully developed pipe profile. However, according to the UPC work presented below, such a profile is not appropriate for the velocity distribution of the 1 mm nozzle orifice. A ‘top hat’ type exit velocity profile was found to be more appropriate.

Because the focus of this work is on fluid behaviour that may influence jetting performance, rheological models capturing the non-Newtonian behaviour for the very high shear rates (10^3-10^6) of interest need to be considered. There are two computational domains of interest to be modelled, each assuming ‘Karcher Forme1’ nozzle type. Domain (A) is an axisymmetric geometry that is easily compared with theoretical cases, laboratory experiments and simulation results from the literature. Domain (B) is based on the geometry of the experimental rig and has a nozzle entry point offset from the centre that rotates at rates compatible with the intended hybrid drilling technology. In this paper, the effects of drilling fluid and setup conditions on impinging pressures are explored for Domain (A), while the feasibility of modelling a rotating jet is proven for Domain (B).

3. THE IC-FERST NUMERICAL MODEL

IC-FERST, an open-source finite-element CFD model, is used here to model the high-speed water jet. It is a general purpose CFD code capable of modelling a wide range of fluid phenomena involving single and multiphase flows. The IC-FERST project’s history has led to several novel advanced methods based upon adapting and moving anisotropic unstructured meshes, and advanced combined finite element and control volume (CVFEM) discretisation. For this rotary jet drilling application, rotation and further non-Newtonian behaviour features were implemented. In the ORCHYD project, drilling fluids and water are treated as incompressible fluids. The temperature has a small effect on water density, i.e., water density decreases from 1000 kg/m^3 to 988 kg/m^3 when the temperature increases from 20°C to 50°C, resulting in 1.2% difference. In this work, we use constant density, 1000 kg/m^3. Important attributes of IC-FERST for this application include *Mesh Adaptivity* and the *Turbulence Model.*

To reduce CPU cost without loss of accuracy, the dynamic mesh adaptivity can be used for application of HPWJ. The grid adaptation scheme used here is based

on the anisotropic grid optimization library of Pain et al. (2001), in which two different techniques can be combined to change elements: mesh refinement or "h" method; and node relocation or "r" method. In this study, we used it for dynamic mesh optimisation (DMO). We also used an adaptive time-step scheme to dynamically adjust the size of the time-step. The size of the time-step is linked to the Courant-Friedrichs-Lewy (CFL) number.

To deal with turbulent flow and associated numerical instabilities, an implicit sub-grid scale filtering through a Smagorinsky's model (Smagorinsky, 1963) is used to discretise the momentum equations. An explicit Large-Eddy Simulation (LES) turbulence model is also implemented within the adaptive meshing approach of the modelling framework; while considering the variability of the adaptive mesh element spatial dimensions, the filter is additionally allowed to vary in space and time. Additionally, in order to add further stabilisation, the Petrov-Galerkin method (Tezduyar, 1991; Pain et al. 2001, Hughes and Mallet, 1986) is also applied to the momentum equations, using an upwind weighting of the equations and an additional diffusion term in the direction of the gradient of the solution.

4. VALIDATION STUDY – DATA FOR A DEEP WIDE DOMAIN (JASPER ET AL., 2021)

The fluid domain of the long pipe problem of Jasper et al. (2021) (length 0.13m, diameter 0.13m) is initially filled with fluid with a pressure of zero and has a boundary condition of p=0 at the outlet (yellow circular area in Fig.1a). A bell-shaped velocity boundary condition with the profile given in Figure 20 is applied at the orifice (orange circular area in Fig.1a) and maintained during the simulation, once started. The rest of the boundaries are applied with no-slip boundary conditions. Fig.1b shows about 30 mm length of the submerged jet showing the shape transitioning from steady core to turbulent eddies and breakdown at 440 µs. All elements for which water velocities are smaller than 10 m/s have been excluded.

Figure 2 demonstrates the simulation of a HPWJ based on an adaptive mesh optimisation which refines the mesh according to the fluid velocity gradient. The minimum mesh edge length is 0.1 mm and the maximum mesh edge length is 5 mm. The fluid mesh used by the IC-FERST code is very refined near the fluid jet and vortices, and relatively coarse elsewhere. We can divide the jet into three zones: (a) jet axial velocity remains nearly constant 320m/s. In this zone, (H/D ≤ ~7) the jet keeps maximum kinetic energy and would generate maximum impinging pressure if it impacts the rock surface; (b) jet axial velocity decreases slightly as small vortices around it affect it. In this zone, jet axial velocity becomes unstable and cannot maintain maximum impinging pressure; (c) jet axial velocity decreases sharply, and the jet turns into more vortices. These results are based on a fully developed profile on entry into the domain.

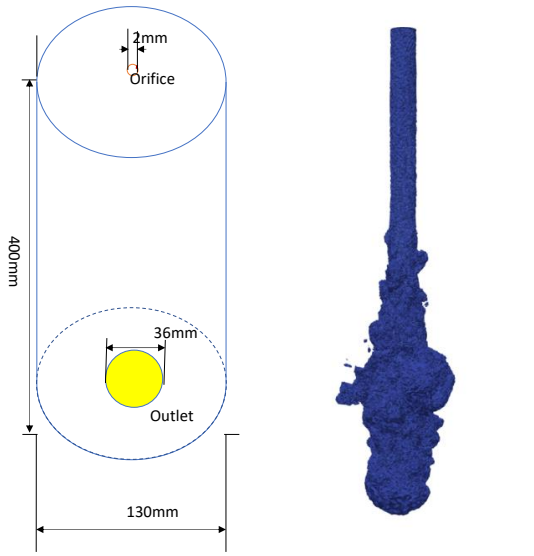

Figure 1: IC-FERST (a) Schematic of simulation setup; (b) jet shape after removal of all elements for which the fluid velocities are less than 10 m/s.

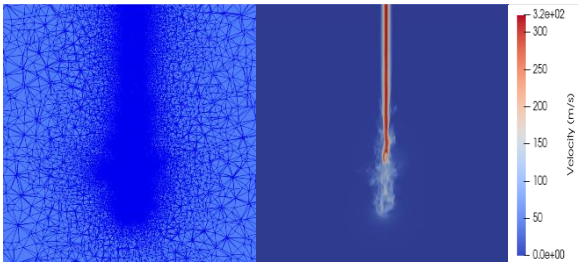

Figure 2: Water jet velocity (right) and mesh adapting around jet (left) at time 440 µs.

The conical jet results from Jasper et al. give the accelerating decline in peak velocity in the jet core with axial distance. With a conical nozzle of 2 mm diameter and with no cavitation, the experimental plot shows that after 14 mm (x/d = 7), the centreline velocity has reduced by about 25-30% which is substantially more than in the jet simulated with IC-FERST. The nozzles in the two cases have different convergence angles and the Re values are different which might explain the discrepancy.

5. APPLICATIONS

5.1 Fixed HPWJ - Domain (A): Impinging Pressure

The main aim is to investigate the effects of HPWJ parameters on impinging pressure, i.e. nozzle diameter, orifice exiting velocity, stand-off distance, and to check any consequences of the fluid viscous properties of water and drilling fluids with the additive graphene oxide (GO). We designed a simple fixed jet test. It is important to realise that we are not sampling flows at different distances from the jet outlet for the case with a jet emerging into a large open domain. Here, the domain available for flows is restricted as the stand-off distance is the solid boundary in front of the jet. The domain above the specimen (light blue part in Fig. 3) is initially filled with fluid with a pressure of zero and has

a boundary condition of p=0 at the circumferential and top boundaries (except the orange circular area for the fluid jet inflow with the specified velocity profile and the yellow annulus area with a no-slip condition at the top boundary). Project partner, UPC used their CFD code to simulate the flow inside the nozzle with different chamber pressures and they extracted the orifice-exiting velocity distribution in the radial direction (Fig. 4). A bi-function is derived to perform curve-fitting and this was applied at the orifice as a velocity boundary condition and maintained during the simulation once started.

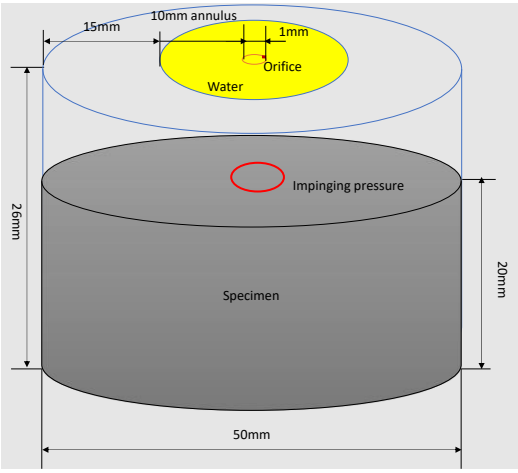

Figure 3: Schematic of simulation setup for Domain A

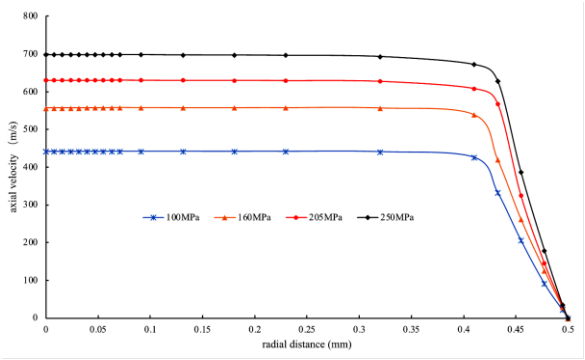

Figure 4: Orifice exiting velocity profile along radial direction as derived from CFD models of UPC (CUP Orchyd Internal Report - "Nozzle simulation results", July 2021). 'Top-hat' profile obtained for 1 mm orifice nozzle 'Karcher Forme1'

The impinging plate pressure profile stabilises before t = 200 ms. For a chamber pressure of 100 MPa, the maximum velocity is 441 m/s and the velocity profile in Fig. 4 is set as the velocity boundary condition and ramped up from 0 m/s to 441 m/s linearly within 80 µs. After the jet impacts the bottom surface, the impinging pressure overshoots the maximum value of 99 MPa at 90 µs and was found to stabilise at 96.9 MPa.

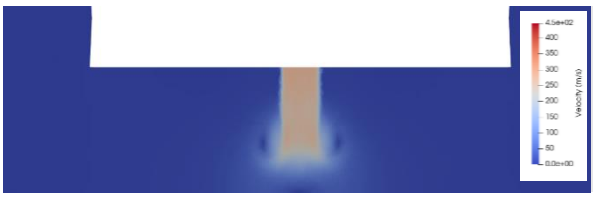

(a) Time 50 µs

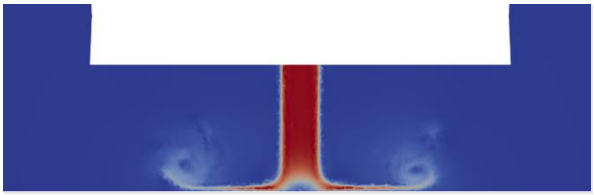

(b) Time 100 µs

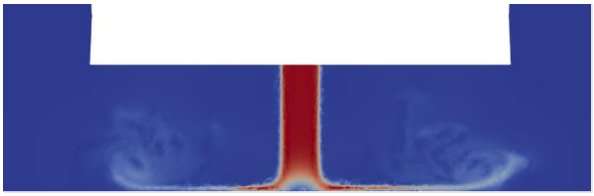

(c) Time 150 µs

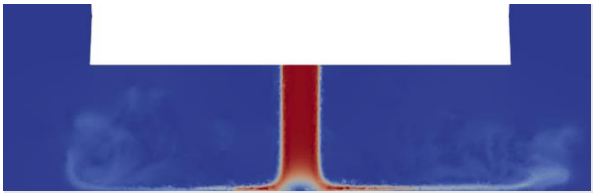

(d) Time 200 µs

(e) Time 200 µs

Figure 5: (a-d) Evolution of fluid velocity for HPWJ with nozzle diameter 1 mm, stand-off distance 3 mm and chamber pressure 100 MPa, (e) Pressure at 200 µs

Fig. 6 shows the impinging pressure on the impinging surface and distribution along x direction. The core pressure contour (arbitrarily plotted here as >95% chamber pressure) is not perfectly circular and the width of this >95% zone is about 0.3 mm.

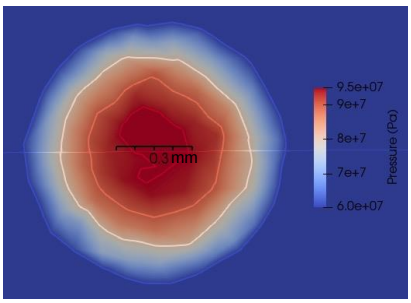

Figure 6: Pressure contours of the impinging bottom surface of the jet in Fig. 5

Fig. 7 shows the distribution of normalised velocity V/Vb along the jet centreline, where Vb is the bulk (i.e., average) velocity through the orifice. Here, we plot horizontal profiles at different distances from the plate (height z=0) up to nozzle at z=3 mm. From the height of z=3D to z=1D, (where D=1 mm) the velocity remains constant in the core region. The velocity in the impinging zone decreases quickly from z=1D to z=0.05D. This agrees with the simulation results published in Wang et al., (2020).

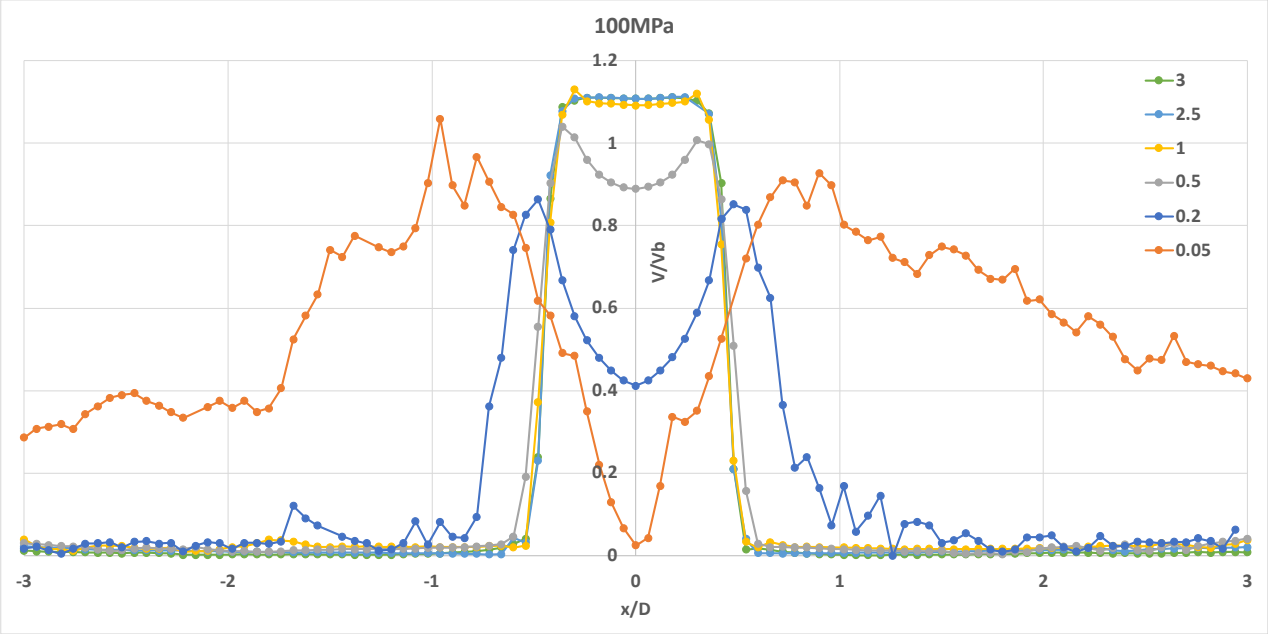

Figure 7: Radial profile development of the normalized mean axial velocity V/Vb at stand-off distance 3 mm (H/D = 3)

5.2 Effect of chamber pressure on impinging pressure

Table 1: Comparison of the numerical results of impinging pressure (in MPa) between ICL and UPC, for stand-off distance = 3D

Chamber pressure	100	160	205	250
ICL numerical results	96.9	155.5	198.5	244.5
UPC numerical results	97	154	198	241

Four numerical tests were undertaken for different chamber pressures: 100 MPa, 160 MPa, 205 MPa, and 250 MPa. The corresponding impinging pressures are shown in Table 1. It shows the impinging pressure increases when the chamber pressure increases. UPC also modelled the axisymmetric case with identical boundary constraints and geometry as shown in Fig. 3. They match each other very well.

5.3 Effect of stand-off distance on impinging pressure

We also investigate the effect of stand-off distance, SD on impinging behaviour for a jet with chamber pressure 100 MPa, and nozzle diameter 1 mm. For SD of 3 mm and 6 mm, the impinging pressures quickly converge to an almost constant value. However, for SD of 10 mm, the impinging pressure keeps fluctuating as vortices which are generated near the impinging area affect the velocity field. If we calculate average impinging pressure using the last four points and plot them, we observe (Fig. 8) the impinging pressure for SD = 3 mm and 6 mm are almost the same but drop to 92.5 MPa for SD of 10 mm.

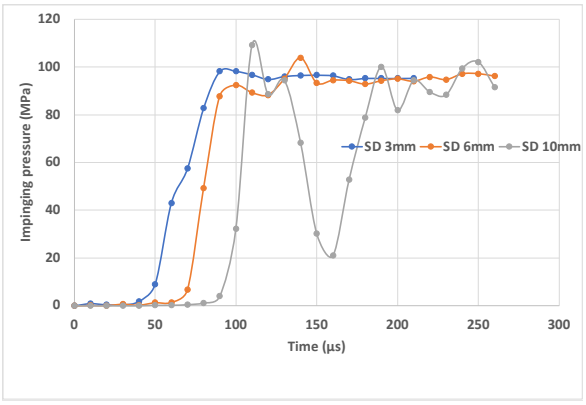

Figure 8: Evolution of impinging pressure for SD 3 mm, 6 mm, and 10 mm

5.4 Effect of nozzle diameter

Constant Chamber Pressure Case.

Diameter of the nozzle is a significant factor which affects the impinging behaviour of the jet. To investigate this effect for SD 3 mm, we choose three diameters of the nozzle, 1 mm, 0.8 mm, and 0.5 mm for the jet with calculated exit velocity distribution associated with velocities for chamber pressure of 100 MPa simulated by UPC. In the work reported here in Section 5.4, first, the same chamber pressures and therefore the same velocity distributions (as a function of normalised diameter) are considered for each of the three nozzle diameters. The three different nozzle orifice diameters lead to three different discharge volumetric flow rates and therefore different pump power. Fig. 9 shows the impinging pressure on the impinging surface and the distribution in the radial (x) direction for orifice diameter 0.8 mm and 0.5 mm. It is notable that the core impinging pressure contours (>95% chamber pressure) are not circular and symmetric, the width of this core zone decreases from 0.3 mm to 0.1 mm when the orifice diameter decreases from 1 mm to 0.5 mm (compare Fig. 6 and Fig. 9).

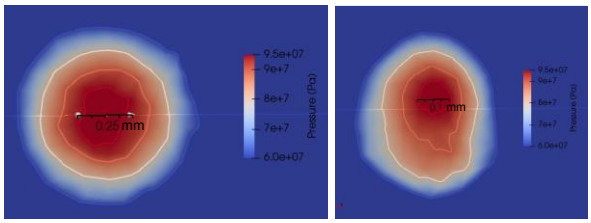

Figure 9: Pressure contours for constant pressure case. Left: 0.8 mm, Right: 0.5 mm

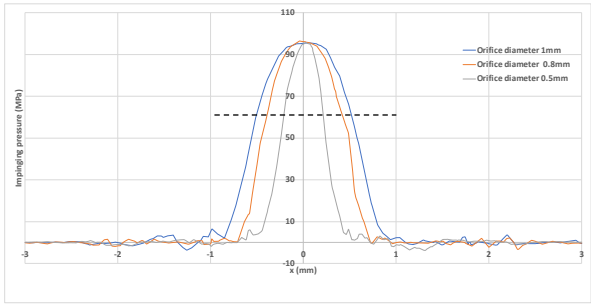

Figure 10: Pressure distribution along the x direction of the impinging plate surface

Figure 10 shows the impinging pressure distribution along the x direction for orifice diameter 1 mm, 0.8 mm and 0.5 mm. The maximum values for the three orifices are almost the same, but the core impinging pressure zone becomes narrower when the orifice diameter decreases from 1 mm to 0.5 mm. Further investigation is included below to explore the effect on inlet velocity and impinging pressure of a reduced nozzle diameter for the same jet power.

Constant Jet Power Case.

In this section, to further investigate the effect of nozzle diameter, we choose two diameters of the nozzle, 1 mm, and 0.8 mm but here each jet is created with the same pump power. For the 1 mm nozzle, we use the same condition described in Section 5.1, i.e., a chamber pressure of 100 MPa, and the appropriate velocity distribution associated with chamber pressure of 100 MPa determined by UPC. This average velocity is 398.6 m/s, and we again consider the impinging pressure for SD of 3 mm. Using Data supplied from Karcher nozzle technical manual, we calculate the pump power as 31.31 kw for this jet. Fig.12 shows the impinging pressure distributions acting radially and along the x direction for orifice diameters of 0.8 mm and 1 mm. The maximum impinging pressure for 0.8 mm and 1 mm are about 127 MPa and 97 MPa respectively. The impinging pressure distribution becomes narrower when the orifice diameter decreases from 1 mm to 0.8 mm (see Figs. 11 and 12). As the 0.8 mm nozzle produces a much higher maximum impinging pressure, it will have generated more destructive power when the jet impacts the rock.

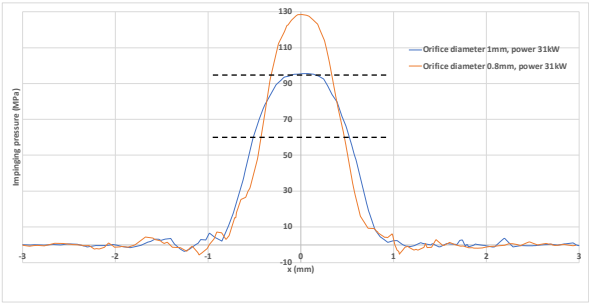

Figure 11: Pressure distribution along the x direction on the bottom impinging plate surface, highlighting 60 MPa and 95 MPa contours.

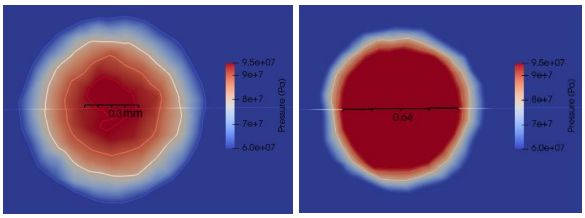

Figure 12: Impinging pressure contours highlighting 95 MPa (red) and 60 MPa (blue) for constant pump (or intensifier) power case, Left: diameter = 1.0 mm, Right: diameter = 0.8 mm, for same stand-off distance SD = 3 mm

These simulations suggest that if equal jet power is available from the intensifier with a slightly smaller diameter nozzle orifice, that a slightly smaller area on the impinging plate is exposed to pressures of 60 MPa. But if we were to set a hypothetical threshold pressure level for which rock damage starts to become appreciable at say, 95 MPa, the area suffering damage is at least 4 times greater for the 0.8 mm diameter jet. If

that threshold were set precisely at say, 120 MPa, only the 0.8 mm diameter jet would generate any rock destruction and for this theoretical case the damage zone would be about 0.4 mm wide. None of this hypothetical discussion takes account of any real rock grain structure, but it does illustrate the trends expected and the possibility to model the potentially most advantageous diameter for a given power and stand-off distance, notwithstanding the fact that the jet's force remains greater for the larger diameter nozzle for this constant power case.

5.5 Effect of non-Newtonian fluids

For Newtonian fluids, viscosity is independent of shear rate. For example, water's viscosity remains constant for a constant temperature, 1 mPa.s at 20 °C. But there are many non-Newtonian fluids which show different behaviour, e.g., in drilling fluids with additive, the viscosity at low shear rates is significantly higher than for water but decreases when shear rate is higher, see Fig. 13. After ensuring a satisfactory extrapolation of viscosity to high shear rates of ~10^6, see Fig. 14, the range of drilling fluids tested with different temperatures and percentage of additives was found to have no influence on impinging pressures and hence jet destruction of rock, see Fig 15.

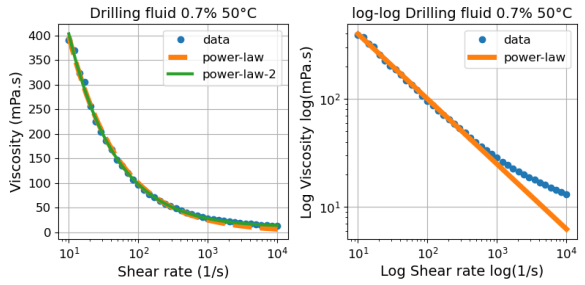

Figure 13: Effective viscosity vs shear rate (blue dot line) and approximation by power law (orange line) and double power law (green line) (provided by Sintef Laboratory)

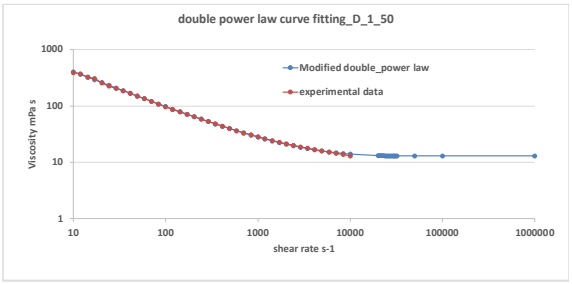

Figure 14: Curve-fitting and extrapolating of experimental data for drilling fluid with 1% additives

5.6 Rotating nozzle simulation for Laboratory Rig - Domain (B)

For nozzles rotating with the drill bit, the rotating speed will influence the jettability of jock. To improve the ability to optimise the set up for improved groove cutting under the action of a rotating jet, a rotating jet computational model (Domain B) has been designed (see Fig. 16) to closely match the experimental setup in the ARMINES laboratory (Fig. 19). The domain is initially filled with fluid with a pressure of zero and has a boundary condition of p=0 at the circumferential and top boundaries (except the red circular area for the fluid jet inflow with the specified velocity profile and the blue annulus area with a no-slip condition at the top boundary).

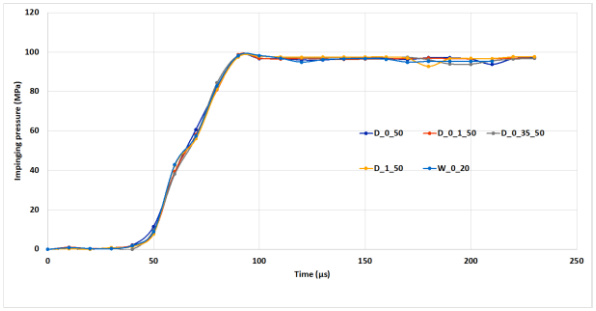

Figure 15: Evolution of impinging pressure for SD of 3 mm

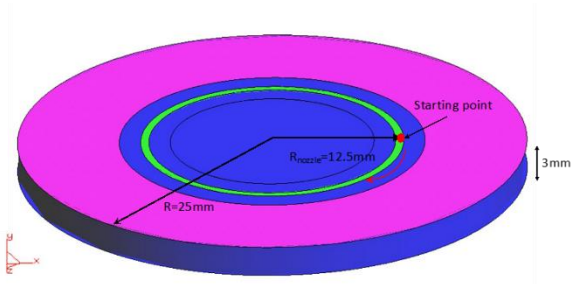

Figure 16: Schematic of simulation setup

The code, IC-FERST, allows users to insert user-defined functions with time via a Python script. Fig. 17 presents a water velocity vector plot around the jet. When two points (Point A. 0.01240, 0.0, 0.001567; Point B. 0.01228, 0.0, 0.002342) in the impinging zone along the path of the nozzle are selected, the resulting impinging pressure plot is as shown in Fig. 18. We can see two very similar pressure pulse signals which appear one after another, point B lags 500 µs behind point A.

6. LABORATORY EXPERIMENTS

6.1 Preliminary results from Pressure Sensor

The experimental setup for HPWJ testing of peripheral groove cutting of rotating rock specimens under confining pressures and back pressure in the ARMINES laboratory is shown in Fig. 19. The rock specimen was fixed on a turntable plate, placed within a confining cell, and is then subject to a confining pressure that can go up to P = 50 MPa, applied by drilling fluid. In order to ensure the correct position of the high pressure nozzle, the high pressure tube can be moved vertically with an accuracy of 0.1 millimetre. The simulated fluid domain (Domain B, Fig. 16) is indicated. A new sensor has been designed and developed by ARMINES in collaboration with a French

company Sixaxes. It allows the measurement at high frequency (more than 10 kHz) of the force of the jet on a 5 mm diameter surface in a pressurized environment up to 50 MPa.

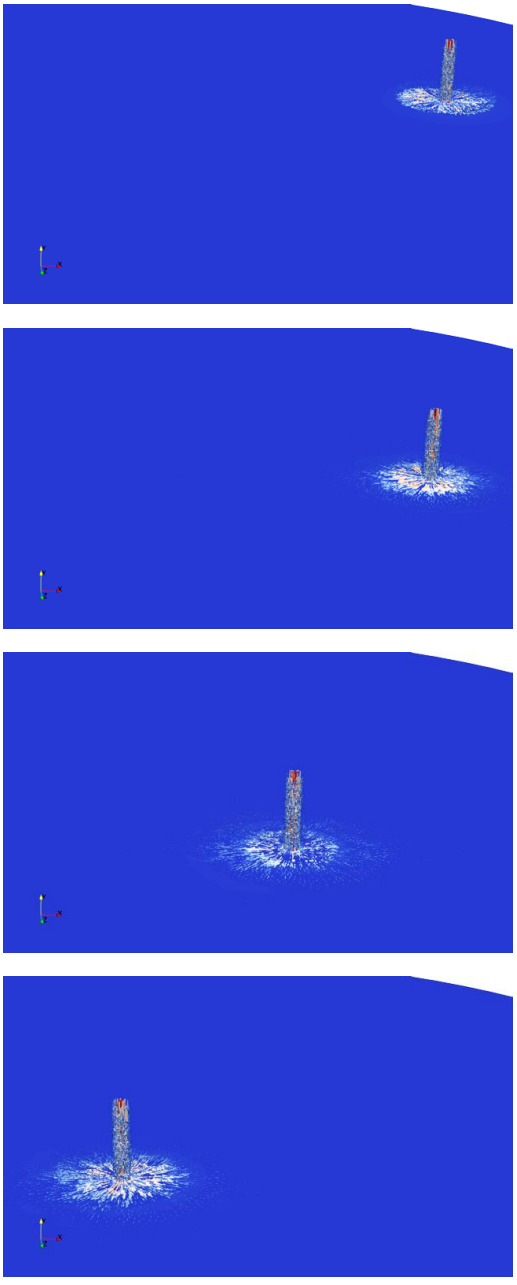

Figure 17: 3D visualisation of the rotating traverse of the jet acting on the base of the domain showing velocity vector plot (top to bottom) at t=0.2 ms, 5 ms, 10 ms, 14 ms.

In order to measure only the effect of the impact of the jet in a confined environment subject to pressure fluctuations (the control of the pressure in Domain B is carried out by an automatic valve which makes it possible to maintain a constant pressure at ± 1 MPa), the sensor is equipped with a system for balancing the pressures by means of a tube filled with silicone, which makes it insensitive to the differences in pressure. The novel pressure sensor is shown in Fig. 20 and is fixed on the turntable (instead of the rock) with an adjustable radius.

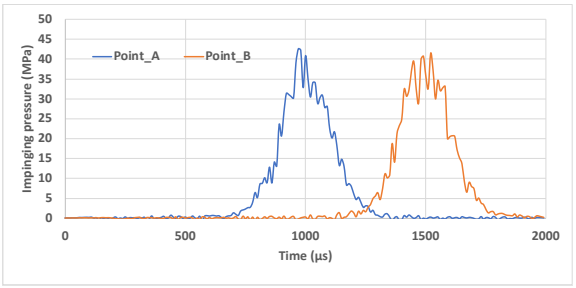

Figure 18: Evolution of impinging pressure at points A and B that lie on the path of a rotating jet traversing on a circular trajectory mimicking the rotating bit.

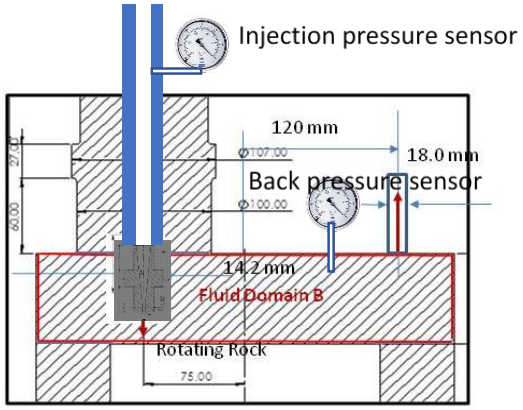

Figure 19: Layout of HPWJ rig in ARMINES laboratory showing impinging point at tip of red arrow together with modelled Domain B.

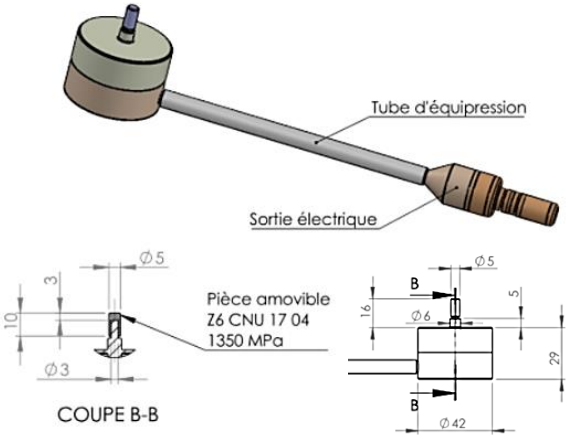

Figure 20: Rugged Very High Pressure Sensor designed in ARMINES, with 5 mm diameter sampling head, ~5 times jet diameter.

Results from the sensor are shown in Fig. 21 suggesting a nonuniform non-symmetric impinging force as the jet's path moves across the sensor boundary, ranging from about 55-135 N with some high frequency fluctuations reaching near to 150 N. The spatial average pressure on the sensor head over a period of time represented by the plateau of about 135 N is 6.88 MPa.

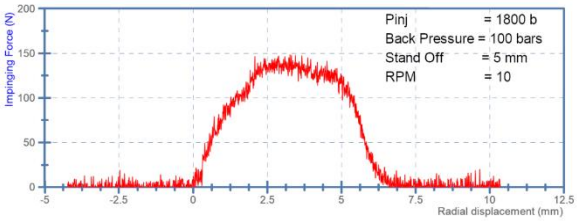

Figure 21: Impinging Force with time output from sensor for ~12 mm arc traversed; back pressure subtracted

Consider now the simulation results, an equivalent virtual experiment, as shown modelled in Fig. 22. Here, the summed forces integrated over the full sensor area are more variable, with a clear plateau of about 150 N but with the numerical simulation capturing high frequency excursions as large as 300 N. The reason that the equivalent plateau force (150 N) and sensor pressure (7.64 MPa) is 11% higher in simulated results than measured by the experimental sensor will be investigated further. In future it will be possible to estimate with reasonable accuracy the peak impinging pressure from measurement made by the 5 mm diameter experimental sensor's average force and pressure values using idealised impinging pressure distributions obtained through simulations such as shown in Fig. 10. In this way it should be possible to deduce from the sensor, maximum impinging pressures and average pressures acting over small impinging areas associated with different nozzle orifice diameters, when the chamber pressures are unsteady or unknown.

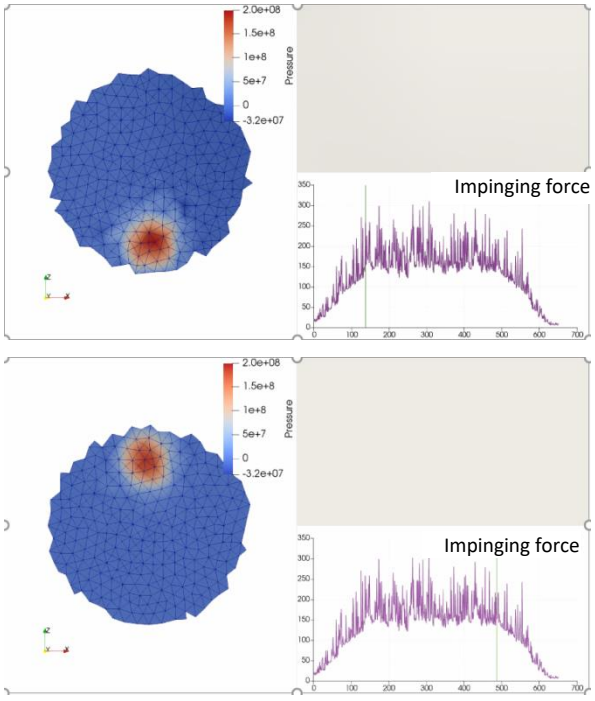

Figure 22: IC-FERST simulation of integrated impinging pressure over an area equivalent to the 5 mm sensor head. Early and late stages of the traverse of the 1 mm jet moving across sensor location at 10 RPM.

6.2 Preliminary results for HPWJ grooving in rock

Preliminary HPWJ tests on granites show that a high chamber pressure minus back pressure of ~170 MPa likely to generate maximum impinging pressures of 90 to 95% of this value for the 1 mm nozzle orifice and slow (4 RPM) rotation and traverse speed will generate a broad groove and rock removal with the selected nozzle and jet operating at a 4 mm stand-off distance. The two granites have quite similar strength properties while the Sidobre with larger grain size than Kuru Grey shows deeper wider grooving with larger chippings. It is interesting to note that two rocks with equivalent compressive strengths undergo completely different cuts. This point, as well as the influence of jet parameters such as injection pressure, back pressure, travelling speed, stand-off distance will be studied in more detail in the next test campaign.

Figure 23: Different susceptibilities of two granite specimens of ~200 mm across (Left: Sidobre, Right: Kuru Grey) to HPWJ grooving as rock specimen rotates under the jet with 180 MPa of HPWJ chamber pressure, 10 MPa back pressure, 4 mm stand-off distance and 4 RPM rotation speed. The nozzle is Karcher forme 1 of 1.0 mm orifice.

7. DISCUSSION AND CONCLUSIONS

The jet simulation results qualitatively match published experimental results (Jasper, et al., 2020). For this simulated case of a nearly infinite domain, the jet keeps maximum kinetic energy in the core zone (H/D from 0 to 7). The jet axial velocity notably reduces when H/D is greater than 7. Therefore, in practice the results for a long wide domain would suggest the stand-off distance should be smaller than 7D to maximise jet energy. Jasper et al. only carried out their experiments under lower Reynolds number (163,000–180,000) and with a different nozzle, so to compare with our numerical tests (Re: 320000-700000), though informative, is not a sound basis for validation especially as it does not address short distances between jet and plate.

If we take the impinging surface into account in defining the domain geometry, the impinging pressure values for each stand-off distance will differ from those suggested by an infinite domain, because the flows are different. Interestingly, for the case H=10D, the largest domain considered, our results agreed closely with UPC's results using an alternative CFD scheme. Preliminary research using the new sensor gives an ~11% difference in simulated impinging force compared with experiments.

The model results for water are consistent with previous work. Impinging pressure in the core increases with chamber pressure and with small percentage reductions in magnitude. For jets with nozzle chamber pressure of 100 MPa, and nozzle diameter 1 mm the impinging pressure quickly converges to an almost constant distribution and average value for stand-off distances of 3 mm and 6 mm, but for stand-off distance 10 mm, the flow is unstable. Results suggest for a 100 MPa chamber pressure, the area of impingement of significantly high-pressure (>95 MPa) found for the 1.0 mm nozzle will be greatly reduced for the 0.5 mm nozzle. The effect of nozzle diameter considered for the case with constant power delivered from the nozzle, shows very clearly the advantage of higher velocities through the nozzle with much higher pressures then focussing over a somewhat reduced area of potential rock destruction.

Jetting with five fluid rheology models with density range of < 2% was simulated to explore the possible extreme effects of different fluids: drilling fluids at 50ºC, with 0%, 0.1%, 0.35% 0.70% and 1% additives, and water at 20 ºC. Numerical results show that impinging pressure is not sensitive to the viscosity changes, which is consistent with the very high Re number regime.

The maximum effective dynamic pressure in the preliminary jetting tests was calculated to be approximately 95% of the difference between chamber pressure and back pressure. This was equal to about 160 MPa and was just sufficient to generate grooves in hard rock with a slow rotation of 4 RPM.

To inform ORCHYD's experimental campaign of direct groove cutting HPWJ tests, a fluid-solid interaction computational framework is being tested and will be reported in future work. It will be used to help assign the most destructive jet configuration and to supplement and extend the realm of deep in-situ stress and bottom hole back pressure conditions beyond the limits possible in the ARMINES laboratory.

REFERENCES

Bobo R. Method of drilling with high velocity jet cutter rock bit. Patent. United States, Patent Office; 1963

Dehkhoda, S., Hood, M., 2013. An experimental study of surface and sub-surface damage in pulsed water-jet breakage of rocks. International Journal of Rock Mechanics and Mining Sciences 63, 138–147.

Hughes, T.J.R. Mallet, M. 1986. A new finite element formulation for computational fluid dynamics: IV. a discontinuity-capturing operator for multidimensional advective-diffusive systems, Comput Methods Appl Mech Eng, 58 (3) 329-336.

Hussein, H.J., Capp, S.P., George, W.K., 1994. Velocity measurements in a high-Reynolds-number, momentum-conserving, axisymmetric, turbulent jet. J. Fluid Mech. 258, 31–75.

Jasper, S., Hussong, J., Lindken, R., 2021. PIV investigation of high Reynolds number submerged water jets at high-pressure ambient conditions. Exp Fluids 62, 97.

Jegaraj, J.J.R., Babu, N.R., 2016. Condition Monitoring of Orifice in Abrasive Waterjet Cutting System Using High Pressure Sensor. Procedia Manufacturing 5, 578–593.

Kolle JJ., 1987. Jet kerfing parameters for confined rock. In: Proceedings of the fourth U.S. Water Jet Conference. Berkeley. 26-28 August: 134–144.

Liao, H., Guan, Z., Shi, Y., Liu, Y., 2015. Field tests and applicability of downhole pressurized jet assisted drilling techniques. Int Journal of Rock Mechanics and Mining Sciences 75, 140–146.

Pain, C., Umpleby, A., De Oliveira, C., Goddard, A., 2001. Tetrahedral mesh optimisation and adaptivity for steady-state and transient finite element calculations. Comp Meth in Applied Mechanics and Engineering 190, 3771–3796.

Poláček, J., Janurová, E., 2017. Impact of pressure of surrounding medium on plain water jet cutting of rocks. Int J Adv Manuf Technol 90, 2185–2191.

Schlichting H, Gersten K. Grenzschicht-Theorie. 9th ed. Berlin Heidelberg: Springer; 1997.

Smagorinsky, J., 1963. General circulation experiments with the primitive equations: I. the basic experiment, Mon Weather Rev 10.1126/science.27.693.594

Stoxreiter, T., Martin, A., Teza, D., Galler, R., 2018. Hard rock cutting with high pressure jets in various ambient pressure regimes. International Journal of Rock Mechanics and Mining Sciences 108, 179–188.

Tezduyar, T.E., 1991. Stabilized finite element formulations for incompressible flow computations, Advances in Applied Mechanics, 28, 1-44.

Wang, H., Qian, Z., Zhang, D., Wang, T., Wang, C., 2020. Numerical Study of the Normal Impinging Water Jet at Different Impinging Height, Based on Wray–Agarwal Turbulence Model. Energies 13, 1744.

Acknowledgement

This project was funded by the European Union's Horizon 2020 research and innovation programme under grant agreement no. 101006752.